arXiv:1006.3591v1 [cond-mat.str-el] 18 Jun 2010

Dynamical coherent-potential approximation approach to excitation spectra in 3d transition metals*

Y. Kakehashi,† M. Atiqur R. Patoary, and T. Tamashiro
Department of Physics and Earth Sciences, Faculty of Science,
University of the Ryukyus, 1 Senbaru, Nishihara, Okinawa, 903-0213, Japan
(Dated: June 21, 2010)

First-principles dynamical CPA (Coherent-Potential Approximation) for electron correlations has been developed further by taking into account higher-order dynamical corrections with use of the asymptotic approximation. The theory is applied to the investigations of a systematic change of excitation spectra in 3*d* transition metals from Sc to Cu at finite temperatures. It is shown that the dynamical effects damp main peaks in the densities of states (DOS) obtained by the local density approximation to the density functional theory, reduce the band broadening due to thermal spin fluctuations, create the Mott-Hubbard type bands in the case of fcc Mn and fcc Fe, and create a small hump corresponding to the '6 eV' satellite in the case of Co, Ni, and Cu. Calculated DOS explain the X-ray photoelectron spectroscopy data as well as the bremsstrahlung isochromat spectroscopy data. Moreover, it is found that screening effects on the exchange energy parameters are significant for understanding the spectra in magnetic transition metals.

PACS numbers: 71.20.Be,78.20.Bh,75.10.Lp,78.70.En

I. INTRODUCTION

Electron correlations play an important role for understanding the electronic structure, magnetism, metal-insulator transition , and the high-temperature superconductivity in the solid-state physics, and thus a large number of theories have been proposed to describe correlated electron systems[1]. Especially, in the case of magnetism, theories of electron correlations have been developed over fifty years to explain the ferromagnetism of transition metals, since the Hartree-Fock approximation was recognized to overestimate their magnetic ordering energy.

Gutzwiller[2–4] proposed a variational theory which takes into account on-site correlations by controlling the probability amplitudes of doubly occupied states, and showed that electron correlations much instabilize the ferromagnetism. Hubbard[5,6] developed a Green function method making use of the equation of motion method and a decoupling approximation that leads to an alloy-analogy picture. He succeeded in describing the metal-insulator transition as well as the instability of ferromagnetism due to electron correlations. Kanamori[7] took into account the multiple scattering of electrons in the low density limit, and showed that the effective Coulomb interaction for the ferromagnetic instability is extremely renormalized by electron-electron interactions.

Above mentioned theories are limited to the ground state. Cyrot[8] extended to finite temperatures an idea of alloy-analogy approximation for electron correlations proposed by Hubbard, on the basis of the functional integral method[9–12]. He explained the T-P phase diagram for metal-insulator transitions qualitatively. Hubbard[13] and Hasegawa[14] independently developed the single-site spin fluctuation theory using the coherent potential approximation (CPA)[15,16]. They showed that thermal spin fluctuations much reduce the Curie temperatures obtained by the Stoner theory for band calculations based on the local density approximation (LDA) to the density functional theory[17].

The single-site spin fluctuation theory reduces to the Hartree-Fock one at zero temperature because it is based on a high-temperature approximation, *i.e.*, the static approximation to the functional integral method. Therefore the theory does not take into account the ground-state electron correlations as found by Gutzwiller, Hubbard, and Kanamori. Kakehashi and Fulde[18] proposed a variational theory which adiabatically takes into account such correlations at finite temperatures, and found further reduction of Curie temperature. Finally, Kakehashi[19] proposed the dynamical CPA which completely takes into account the dynamical charge and spin fluctuations within the single-site approximation, and clarified the dynamical effects on the momentum distribution, magnetic moment as well as excitation spectra using the Monte-Carlo technique. In the next paper[20] which we refer to I in the following, we developed an analytic method to the dynamical CPA, using the harmonic approximation. In the recent paper[21] which we refer

* To be published in Phys. Rev. B.

to II, we proposed the first-principles dynamical CPA which combines the dynamical CPA with the tight-binding linear-muffintin-orbital (TB-LMTO)[22] base LDA+U Hamiltonian[23]. Within the 2nd-order dynamical corrections to the static approximation, we have shown that the dynamical CPA can describe the finite temperature properties of excitations and magnetism in Fe and Ni quantitatively or semiquantitatively.

In this paper, we develop further the first-principles dynamical CPA by taking into account higher-order dynamical corrections within an asymptotic approximation, and investigate a systematic change of excitation spectra in $3d$ transition metals from Sc to Cu. We will clarify the dynamical effects on the excitation spectra in $3d$ series at finite temperatures, and will explain systematic change of X-ray photoelectron spectroscopy (XPS) data[24] as well as the bremsstrahlung isochromat (BIS) data[25].

Similar calculations have recently been performed at the ground state by Belashchenko *et. al.*[26] on the basis of the self-consistent local GW approximation. Their results of the first-principles calculations, however, do not well describe the main peak positions in the XPS and the BIS data, and seem to require further development of the theory.

As we have proven in the separate papers[27,28], the dynamical CPA is equivalent to the many-body CPA[29] developed in the disordered system, the dynamical mean field theory (DMFT) in the metal-insulator transition in infinite dimensions[30–33], and the projection operator method CPA (PM-CPA)[34] for excitation problems. The dynamical CPA was originally developed to describe the finite-temperature magnetism in metallic systems starting from the static approximation exact in the high-temperature limit. The theory can treat the transverse spin fluctuations for arbitrary d electron number at finite temperatures, though it is not easy in the traditional quantum Monte-Carlo approach (QMC)[35]. Moreover the theory allows us to calculate excitation spectra up to the temperatures much lower than those calculated by the QMC because the dynamical CPA is an analytic theory which does not rely on the statistical techniques.

In the following section, we outline the first-principles dynamical CPA presented in our paper II. After having established the basic formulation, it is desired how to calculate higher-order terms of individual harmonics in the dynamical part. In Sec. III, we calculate the higher-order terms using asymptotic approximation, and obtain the expressions for dynamical corrections. In Sec. IV, we present the results of numerical calculations for the densities of states (DOS) as the single-particle excitations in $3d$ transition metals. Calculations have been performed at high temperatures, where the present approach works best. We will demonstrate that the dynamical CPA can explain a systematic change of the DOS in $3d$ series from Sc to Cu. We also show that the screening effects on the exchange energy parameter are significant for the description of the excitation spectra in Mn, Fe, and Co. In the last section, we summarize the present work and discuss future problems to be solved.

II. FIRST-PRINCIPLES TB-LMTO DYNAMICAL CPA

We consider here a transition metal system with an atom per unit cell, and adopt the TB-LMTO Hamiltonian combined with a LDA+U Coulomb interactions as follows[21].

$$H = H_0 + H_1, \tag{1}$$

$$H_0 = \sum_{iL\sigma} (\epsilon_L^0 - \mu)\, \hat{n}_{iL\sigma} + \sum_{iLjL'\sigma} t_{iLjL'}\, a^\dagger_{iL\sigma} a_{jL'\sigma}\ , \tag{2}$$

$$H_1 = \sum_i \Big[\sum_m U_0\, \hat{n}_{ilm\uparrow}\hat{n}_{ilm\downarrow} + \sum_{m>m'} (U_1 - \frac{1}{2}J)\hat{n}_{ilm}\hat{n}_{ilm'} - \sum_{m>m'} J\hat{\boldsymbol{s}}_{ilm}\cdot\hat{\boldsymbol{s}}_{ilm'} \Big]\ . \tag{3}$$

Here ϵ_L^0 in the noninteracting Hamiltonian H_0 is an atomic level on site i and orbital L, μ is the chemical potential, $t_{iLjL'}$ is a transfer integral between orbitals iL and jL'. $L = (l, m)$ denotes s, p, and d orbitals. $a^\dagger_{iL\sigma}$ ($a_{iL\sigma}$) is the creation (annihilation) operator for an electron with orbital L and spin σ on site i, and $\hat{n}_{iL\sigma} = a^\dagger_{iL\sigma}a_{iL\sigma}$ is a charge density operator for electrons with orbital L and spin σ on site i.

In the Coulomb interaction term H_1, we take into account on-site interactions between d electrons ($l = 2$). U_0 (U_1) and J in H_1 are the intra-orbital (inter-orbital) Coulomb and exchange interactions, respectively. $\hat{n}_{ilm}$ ($\hat{\boldsymbol{s}}_{ilm}$) with $l = 2$ is the charge (spin) density operator for d electrons on site i and orbital m. It should be noted that the atomic level ϵ_L^0 in H_0 is not identical with the LDA atomic level ϵ_L. The former is given by the latter as[23,36] $\epsilon_L^0 = \epsilon_L - \partial E^U_{\rm LDA}/\partial n_{iL\sigma}$. Here $n_{iL\sigma}$ is the charge density at the ground state, $E^U_{\rm LDA}$ is a LDA functional to the intraatomic Coulomb interactions.

The free energy of the system $\mathcal{F}$ is written in the interaction representation as follows.

$$e^{-\beta\mathcal{F}} = \mathrm{Tr}\left[\mathcal{T}\exp\left(-\int_0^\beta (H_0(\tau)+H_1(\tau))\right)\right]. \tag{4}$$

Here β is the inverse temperature, $\mathcal{T}$ denotes the time-ordered product for operators. $H_0(\tau)$ ($H_1(\tau)$) is the interaction representation of Hamiltonian H_0 (H_1).

We transform the interaction $H_1(\tau)$ in the free energy into a one-body dynamical potential v making use of the Hubbard-Stratonovich transformation[12,21]. The transformation is a Gaussian formula for the Bose-type operator $\{b_\mu\}$.

$$\mathrm{e}^{\sum_{mm'} b_m \bar{A}_{mm'} b_{m'}} = \sqrt{\frac{\det\bar{A}}{\pi^M}}\int[\prod_m dx_m]\ \mathrm{e}^{-\sum_{mm'}(x_m\bar{A}_{mm'}x_{m'}-2b_m\bar{A}_{mm'}x_{m'})}. \tag{5}$$

Here $\bar{A}_{mm'}$ is a $M\times M$ matrix, and $\{x_m\}$ are auxiliary field variables. The above formula implies that the two-body interaction $\sum_{mm'} b_m\bar{A}_{mm'}b_{m'}$ is transformed into a one-body interaction with a potential $-\sum_{m'} 2\bar{A}_{mm'}x_{m'}$ coupled with the random fields $\{x_{m'}\}$.

After making use of the transformation at each time τ, the free energy $\mathcal{F}$ is written in the Matsubara frequency representation as follows.

$$e^{-\beta\mathcal{F}} = \int\Big[\prod_{j=1}^{N}\prod_{m=1}^{2l+1}\delta\boldsymbol{\xi}_{jm}\delta\zeta_{jm}\Big]\exp\big[-\beta E[\boldsymbol{\xi},\zeta]\big], \tag{6}$$

$$\begin{aligned} E[\boldsymbol{\xi},\zeta] &= -\beta^{-1}\ln\mathrm{Tr}(\mathrm{e}^{-\beta H_0}) - \beta^{-1}\mathrm{Sp}\ln(1-vg) \\ &\quad +\frac{1}{4}\sum_{in}\sum_{mm'}\left[\zeta^*_{im}(i\omega_n)A_{mm'}\zeta_{im'}(i\omega_n)+\sum_{\alpha=x,y,z}\xi^*_{im\alpha}(i\omega_n)B^\alpha_{mm'}\xi_{im'\alpha}(i\omega_n)\right]. \end{aligned} \tag{7}$$

Here N is the number of sites, $\zeta_{im}(i\omega_n)$ ($\xi_{im\alpha}(i\omega_n)$) is the n-frequency component of an auxiliary field $\zeta_{im}(\tau)$ ($\xi_{im\alpha}(\tau)$) being conjugate with $i\hat{n}_{iL}(\tau)$ ($\hat{m}_{iL\alpha}(\tau)=2\hat{s}_{iL\alpha}(\tau)$) for $l=2$. Sp in the second term at the r.h.s. (right-hand-side) of Eq. (7) denotes a trace over site, orbital, frequency, and spin. g is the temperature Green function for noninteracting system H_0. The matrices $A_{mm'}$ and $B^\alpha_{mm'}$ are defined by $A_{mm'}=U_0\delta_{mm'}+(2U_1-J)(1-\delta_{mm'})$, $B^\alpha_{mm'}=J(1-\delta_{mm'})$ ($\alpha=x,y$), and $B^z_{mm'}=U_0\delta_{mm'}+J(1-\delta_{mm'})$.

The functional integrals in Eq. (6) are defined by

$$\int\Big[\prod_{m=1}^{2l+1}\delta\zeta_{im}\Big] = \int\prod_{m=1}^{N'}\sqrt{\frac{\beta^{2l+1}\det A}{(4\pi)^{2l+1}}}\prod_{m=1}^{2l+1}d\zeta_{im}(0)\left[\prod_{n=1}^{\infty}\frac{\beta^{2l+1}\det A}{(4\pi)^{2l+1}}d^2\zeta_{im}(i\omega_n)\right]. \tag{8}$$

Here $d^2\zeta_{im}(i\omega_n)=d\mathrm{Re}\zeta_{im}(i\omega_n)d\mathrm{Im}\zeta_{im}(i\omega_n)$. The dynamical one-body potential v at the r.h.s. of Eq. (7) is defined by

$$(v)_{iLn\sigma jL'n'\sigma'} = v_{jL\sigma\sigma'}(i\omega_n - i\omega_{n'})\delta_{ij}\delta_{LL'}, \tag{9}$$

$$v_{iL\sigma\sigma'}(i\omega_\nu) = -\frac{1}{2}\sum_{m'} iA_{mm'}\zeta_{im'}(i\omega_\nu)\delta_{l2}\delta_{\sigma\sigma'} - \frac{1}{2}\sum_\alpha\sum_{m'}B^\alpha_{mm'}\xi_{im'\alpha}(i\omega_\nu)\delta_{l2}(\sigma_\alpha)_{\sigma\sigma'}, \tag{10}$$

σ_α ($\alpha=x,y,z$) being the Pauli spin matrices.

In the dynamical CPA[20], we introduce a site-diagonal coherent potential

$$(\Sigma)_{iLn\sigma jL'n'\sigma'} = \Sigma_{L\sigma}(i\omega_n)\delta_{ij}\delta_{LL'}\delta_{nn'}\delta_{\sigma\sigma'}, \tag{11}$$

into the potential part of the energy functional $E[\boldsymbol{\xi},\zeta]$, and expand the correction $v-\Sigma$ with respect to sites.

$$E[\boldsymbol{\xi},\zeta] = N\tilde{\mathcal{F}}(\Sigma) + \sum_i E_i[\boldsymbol{\xi}_i,\zeta_i] + \Delta E. \tag{12}$$

Here the zero-th order term $\tilde{\mathcal{F}}(\Sigma)$ is a coherent part of the free energy which is defined by

$$\tilde{\mathcal{F}}(\Sigma) = -(N\beta)^{-1}\ln\mathrm{Tr}(\mathrm{e}^{-\beta H_0}) - (N\beta)^{-1}\mathrm{Sp}\ln(1-\Sigma g)\ . \tag{13}$$

The next term in Eq. (12) is a sum of the single-site energies $E_i[\boldsymbol{\xi}_i, \zeta_i]$. The dynamical CPA neglects the higher-order terms ΔE associated with inter-site correlations.

The free energy per atom is finally given by[20,21]

$$\mathcal{F}_{\mathrm{CPA}} = \tilde{\mathcal{F}}[\Sigma] - \beta^{-1}\ln\int\Big[\prod_{\alpha}\sqrt{\frac{\beta\tilde{J}_\alpha}{4\pi}}d\xi_\alpha\Big]\,\mathrm{e}^{-\beta E_{\mathrm{eff}}(\boldsymbol{\xi})}. \tag{14}$$

Here $\tilde{J}_x = \tilde{J}_y = \tilde{J}_\perp = [1-1/(2l+1)]J$, $\tilde{J}_z = U_0/(2l+1) + \tilde{J}_\perp$, and we expressed the single-site term (the second term at the r.h.s. Eq. (14)) with use of an effective potential $E_{\mathrm{eff}}(\boldsymbol{\xi})$ projected onto a large static field variables $\xi_\alpha = \sum_m \xi_{m\alpha}(0)$. Moreover we have omitted the site indices for simplicity.

The effective potential $E_{\mathrm{eff}}(\boldsymbol{\xi})$ consists of the static contribution $E_{\mathrm{st}}(\boldsymbol{\xi})$ and the dynamical correction term $E_{\mathrm{dyn}}(\boldsymbol{\xi})$.

$$E_{\mathrm{eff}}(\boldsymbol{\xi}) = E_{\mathrm{st}}(\boldsymbol{\xi}) + E_{\mathrm{dyn}}(\boldsymbol{\xi}). \tag{15}$$

The former is given as

$$\begin{aligned} E_{\mathrm{st}}(\boldsymbol{\xi}) \ &= \ -\frac{1}{\beta}\sum_{mn}\ln\Big[(1-\delta v_{L\uparrow}(0)F_{L\uparrow}(i\omega_n))(1-\delta v_{L\downarrow}(0)F_{L\downarrow}(i\omega_n)) - \frac{1}{4}\tilde{J}_\perp^2\xi_\perp^2 F_{L\uparrow}(i\omega_n)F_{L\downarrow}(i\omega_n)\Big] \\ &\quad +\frac{1}{4}\Big[-(U_0-2U_1+J)\sum_m\tilde{n}_L(\boldsymbol{\xi})^2 - (2U_1-J)\tilde{n}_l(\boldsymbol{\xi})^2 + \tilde{J}_\perp^2\xi_\perp^2 + \tilde{J}_z^2\xi_z^2\Big]. \end{aligned} \tag{16}$$

Here $\delta v_{L\sigma}(0) = v_{L\sigma}(0) - \Sigma_{L\sigma}(i\omega_n)$, and $\xi_\perp^2 = \xi_x^2 + \xi_y^2$. $v_{L\sigma}(0)$ is a static potential given by $v_{L\sigma}(0) = [(U_0 - 2U_1 + J)\tilde{n}_{lm}(\boldsymbol{\xi}) + (2U_1 - J)\tilde{n}_l(\boldsymbol{\xi})]/2 - \tilde{J}_z\xi_z\sigma/2$. The electron number $\tilde{n}_L(\boldsymbol{\xi})$ for a given $\boldsymbol{\xi}$ is expressed by means of an impurity Green function as

$$\tilde{n}_L(\boldsymbol{\xi}) = \frac{1}{\beta}\sum_{n\sigma}G_{L\sigma}(\boldsymbol{\xi}, i\omega_n), \tag{17}$$

and $\tilde{n}_l(\boldsymbol{\xi}) = \sum_m \tilde{n}_L(\boldsymbol{\xi})$. The impurity Green function $G_{L\sigma}(\boldsymbol{\xi}, i\omega_n)$ has to be determined self-consistently. The explicit expression will be given later (see Eq. (32)).

The coherent Green function $F_{L\sigma}(i\omega_n)$ in Eq. (16) is defined by

$$F_{L\sigma}(i\omega_n) = [(i\omega_n - \boldsymbol{H}_0 - \boldsymbol{\Sigma}(i\omega_n))^{-1}]_{iL\sigma iL\sigma}. \tag{18}$$

Here $(\boldsymbol{H}_0)_{iL\sigma jL'\sigma}$ is the one-electron Hamiltonian matrix for the noninteracting Hamiltonian H_0, and $(\boldsymbol{\Sigma}(i\omega_n))_{iL\sigma jL'\sigma} = \Sigma_{L\sigma}(i\omega_n)\delta_{ij}\delta_{LL'}$.

The dynamical potential $E_{\mathrm{dyn}}(\boldsymbol{\xi})$ in Eq. (15) has been obtained within the harmonic approximation[20,21,37,38]. It is based on an expansion of $E_{\mathrm{dyn}}(\boldsymbol{\xi})$ with respect to the frequency mode of the dynamical potential $v_{L\sigma\sigma'}(i\omega_\nu)$, where $\omega_\nu = 2\nu\pi/\beta$. The harmonic approximation is the neglect of the mode-mode coupling terms in the expansion. We have then (see Eq. (55) in our paper II)

$$E_{\mathrm{dyn}}(\boldsymbol{\xi}) = -\beta^{-1}\ln\left[1 + \sum_{\nu=1}^{\infty}(\overline{D}_\nu - 1)\right]. \tag{19}$$

Here the determinant D_ν is a contribution from a dynamical potential $v_{L\sigma\sigma'}(i\omega_\nu)$ with frequency ω_ν, and the upper bar denotes a Gaussian average with respect to the dynamical charge and exchange field variables, $\zeta_m(i\omega_n)$ and $\xi_{m\alpha}(i\omega_n)$ $(\alpha = x, y, z)$.

The determinant D_ν is expressed as[21]

$$D_\nu = \prod_{k=0}^{\nu-1}\left[\prod_{m=1}^{2l+1}D_\nu(k,m)\right], \tag{20}$$

$$D_\nu(k,m) = \begin{vmatrix} \ddots & & & & & & \\ & 1 & 1 & & 0 & & \\ & a_{-\nu+k}(\nu,m) & 1 & 1 & & & \\ & & a_k(\nu,m) & 1 & 1 & & \\ & & & a_{\nu+k}(\nu,m) & 1 & 1 & \\ & 0 & & & a_{2\nu+k}(\nu,m) & & \\ & & & & & \ddots & \end{vmatrix} . \tag{21}$$

Note that 1 in the above determinant denotes the 2×2 unit matrix, $a_n(\nu,m)$ is a 2×2 matrix defined by

$$a_n(\nu,m)_{\sigma\sigma'} = \sum_{\sigma''\sigma'''\sigma''''} v_{L\sigma\sigma''}(i\omega_\nu)\tilde{g}_{L\sigma''\sigma'''}(i\omega_n - i\omega_\nu)v_{L\sigma'''\sigma''''}(-i\omega_\nu)\tilde{g}_{L\sigma''''\sigma'}(i\omega_n) \ , \tag{22}$$

$$\tilde{g}_{L\sigma\sigma'}(i\omega_n) = [(F_L(i\omega_n)^{-1} - \delta v_0)^{-1}]_{\sigma\sigma'} \ . \tag{23}$$

Here $v_{L\sigma\sigma'}(i\omega_\nu)$ is defined by Eq. (10). $\tilde{g}_{L\sigma\sigma'}(i\omega_n)$ is the impurity Green function in the static approximation, $(F_L(i\omega_n))_{\sigma\sigma'} = F_{L\sigma}(i\omega_n)\delta_{\sigma\sigma'}$, and δv_0 is defined by $(\delta v_0)_{\sigma\sigma'} = v_{L\sigma\sigma'}(0) - \Sigma_{L\sigma}(i\omega_n)\delta_{\sigma\sigma'}$.

The determinant $D_\nu(k,m)$ is expanded with respect to the dynamical potential as follows.

$$D_\nu(k,m) = 1 + D_\nu^{(1)}(k,m) + D_\nu^{(2)}(k,m) + \cdots \ , \tag{24}$$

$$D_\nu^{(n)}(k,m) = \sum_{\alpha_1\gamma_1\cdots\alpha_n\gamma_n} v_{\alpha_1}(\nu,m)v_{\gamma_1}(-\nu,m)\cdots v_{\alpha_n}(\nu,m)v_{\gamma_n}(-\nu,m)\hat{D}^{(n)}_{\{\alpha\gamma\}}(\nu,k,m) \ . \tag{25}$$

Here the subscripts α_i and γ_i take 4 values 0, x, y, and z, and

$$v_0(\nu,m) = -\frac{1}{2}i\sum_{m'} A_{mm'}\zeta_{m'}(i\omega_\nu)\delta_{l2} \ , \tag{26}$$

$$v_\alpha(\nu,m) = -\frac{1}{2}\sum_{m'} B^\alpha_{mm'}\xi_{m'\alpha}(i\omega_\nu)\delta_{l2} \ , \qquad (\alpha = x,y,z) \ . \tag{27}$$

Note that the subscript $\{\alpha\gamma\}$ of $\hat{D}^{(n)}_{\{\alpha\gamma\}}(\nu,k,m)$ in Eq. (25) denotes a set of $(\alpha_1\gamma_1,\cdots,\alpha_n\gamma_n)$. The frequency dependent factors $\hat{D}^{(n)}_{\{\alpha\gamma\}}(\nu,k,m)$ consist of a linear combination of $2n$ products of the static Green functions. Their first few terms are given in Appendix A of our paper II[21]. Approximate expressions for higher-order terms will be given in the next section.

Substituting Eq. (24) into Eq. (20) and taking the Gaussian average, we reach

$$E_{\rm dyn}(\boldsymbol{\xi}) = -\beta^{-1}\ln\left(1 + \sum_{n=1}^{\infty}\sum_{\nu=1}^{\infty}\overline{D}_\nu^{(n)}\right), \tag{28}$$

and

$$\overline{D}_\nu^{(n)} = \frac{1}{(2\beta)^n}\sum_{\sum_{km} l(k,m)=n}\sum_{\{\alpha_j(k,m)\}}\sum_{\rm P}\prod_{m=1}^{2l+1}\prod_{k=0}^{\nu-1}\left[\Big(\prod_{j=1}^{l(k,m)} C^{\alpha_j(k,m)}_{mm_{\rm p}}\Big)\hat{D}^{(l(k,m))}_{\{\alpha\alpha_{{\rm p}^{-1}}\}}(\nu,k,m)\right]. \tag{29}$$

Here each element of $\{l(k,m)\}$ $(k = 0,\cdots,\nu-1; m = 1,\cdots,2l+1)$ has a value of zero or positive integer. $\alpha_j(k,m)$ takes one of 4 cases 0, x, y, and z. j denotes the j-th member of the (k,m) block with $l(k,m)$ elements. P denotes a permutation of a set $\{(j,k,m)\}$; $\mathrm{P}\{(j,k,m)\} = \{(j_{\rm p},k_{\rm p},m_{\rm p})\}$. $\alpha_{{\rm p}^{-1}}$ means a rearrangement of $\{\alpha_j(k,m)\}$ according to the inverse permutation P^{-1}. The coefficient $C^\alpha_{mm'}$ in Eq. (29) is a Coulomb interaction defined by

$$C^\alpha_{mm'} = \begin{cases} -A_{mm'} & (\alpha = 0) \\ B^\alpha_{mm'} & (\alpha = x,y,z) \ . \end{cases} \tag{30}$$

The coherent potential can be determined by the stationary condition $\delta\mathcal{F}_{\rm CPA}/\delta\Sigma = 0$. This yields the CPA equation as[21]

$$\langle G_{L\sigma}(\boldsymbol{\xi}, i\omega_n)\rangle = F_{L\sigma}(i\omega_n) \ . \tag{31}$$

Here $\langle\ \rangle$ at the l.h.s. (left-hand-side) is a classical average taken with respect to the effective potential $E_{\rm eff}(\boldsymbol{\xi})$. The impurity Green function is given by

$$G_{L\sigma}(\boldsymbol{\xi}, i\omega_l) = \tilde{g}_{L\sigma\sigma}(i\omega_l) + \frac{\displaystyle\sum_n \sum_\nu \frac{\delta\overline{D}_\nu^{(n)}}{\kappa_{L\sigma}(i\omega_l)\delta\Sigma_{L\sigma}(i\omega_l)}}{\displaystyle 1 + \sum_n \sum_\nu \overline{D}_\nu^{(n)}} \ . \tag{32}$$

Note that the first term at the r.h.s. (right-hand-side) is the impurity Green function in the static approximation, which is given by Eq. (23). The second term is the dynamical corrections, and $\kappa_{L\sigma}(i\omega_l) = 1 - F_{L\sigma}(i\omega_l)^{-2}\delta F_{L\sigma}(i\omega_l)/\delta\Sigma_{L\sigma}(i\omega_l)$.

Solving the CPA equation (31) self-consistently, we obtain the effective medium. The electron number on each orbital L is then calculated from

$$\langle \hat{n}_L\rangle = \frac{1}{\beta}\sum_{n\sigma} F_{L\sigma}(i\omega_n) \ . \tag{33}$$

The chemical potential μ is determined from the condition $n_e = \sum_L \langle \hat{n}_L\rangle$. Here n_e denotes the conduction electron number per atom. The magnetic moment is given by

$$\langle \hat{m}_L^z\rangle = \frac{1}{\beta}\sum_{n\sigma} \sigma F_{L\sigma}(i\omega_n) \ . \tag{34}$$

In particular, the $l = 2$ components of magnetic moment are expressed as

$$\langle \hat{\boldsymbol{m}}_l\rangle = \langle \boldsymbol{\xi}\rangle \ . \tag{35}$$

The above relation implies that the effective potential $E_{\rm eff}(\boldsymbol{\xi})$ is a potential energy for a local magnetic moment $\boldsymbol{\xi}$.

III. HIGHER-ORDER DYNAMICAL CORRECTIONS IN ASYMPTOTIC APPROXIMATION

In our previous paper II[21], we took into account the dynamical corrections up to the second order in Eqs. (28) and (32). We will obtain higher-order terms in this section using an asymptotic approximation.

We note that the coupling constants $B^x_{mm'} = B^y_{mm'} = J(1-\delta_{mm'})$ are much smaller than $A_{mm'}$ and $B^z_{mm'}$ because U_0 and $U_1 \gg J$. The latter condition is not necessarily satisfied for Sc and Ti. But J in these elements are small as compared with the d band width. Thus we neglect the transverse potentials, $v_x(\nu, m)$ and $v_y(\nu, m)$ in the higher-order dynamical corrections. This approximation implies that $a_n(\nu, m)_{\sigma-\sigma} = 0$. The determinant $D_\nu(k, m)$ in Eq. (20) is then written by the products of the single-spin components as

$$D_\nu(k, m) = D_{\nu\uparrow}(k, m)D_{\nu\downarrow}(k, m). \tag{36}$$

Here $D_{\nu\sigma}(k, m)$ is defined by Eq. (21) in which the 2×2 unit matrices have been replaced by 1 (*i.e.*, 1×1 unit matrices), and the 2×2 matrices $a_n(\nu, m)$ have been replaced by the 1×1 matrices $a_n(\nu, m)_{\sigma\sigma}$. The latter is now given by

$$a_n(\nu, m)_{\sigma\sigma} = \sum_{\alpha,\gamma}^{0,z} v_\alpha(\nu, m)v_\gamma(-\nu, m)\hat{h}_{\alpha\gamma\sigma}e_{n\sigma}(\nu, m), \tag{37}$$

$$e_{n\sigma}(\nu, m) = \tilde{g}_{L\sigma}(n-\nu)\tilde{g}_{L\sigma}(n). \tag{38}$$

Here $\hat{h}_{\alpha\gamma\sigma} = \delta_{\alpha\gamma} + \sigma(1-\delta_{\alpha\gamma})$, and we used a notation $\tilde{g}_{L\sigma}(n) = \tilde{g}_{L\sigma\sigma}(i\omega_n)$ for simplicity.

With use of the Laplace expansion, the determinant $D_{\nu\sigma}(k,m)$ can be written as

$$D_{\nu\sigma}(k,m) = \tilde{D}_{1\sigma}(\nu,k,m)D_{1\sigma}(\nu,k,m) - a_k(\nu,m)_{\sigma\sigma}\tilde{D}_{2\sigma}(\nu,k,m)D_{2\sigma}(\nu,k,m). \tag{39}$$

Here $D_{n\sigma}(\nu,k,m)$ and $\tilde{D}_{n\sigma}(\nu,k,m)$ are defined by

$$D_{n\sigma}(\nu,k,m) = \begin{vmatrix} 1 & 1 & & 0 & \\ a_{n\nu+k}(\nu,m)_{\sigma\sigma} & 1 & 1 & & \\ & a_{(n+1)\nu+k}(\nu,m)_{\sigma\sigma} & 1 & 1 & \\ & & a_{(n+2)\nu+k}(\nu,m)_{\sigma\sigma} & 1 & 1 \\ & & & & \ddots \\ 0 & & & & \end{vmatrix}, \tag{40}$$

$$\tilde{D}_{n\sigma}(\nu,k,m) = \begin{vmatrix} 1 & 1 & & 0 & \\ a_{-n\nu+k}(\nu,m)_{\sigma\sigma} & 1 & 1 & & \\ & a_{-(n+1)\nu+k}(\nu,m)_{\sigma\sigma} & 1 & 1 & \\ & & a_{-(n+2)\nu+k}(\nu,m)_{\sigma\sigma} & 1 & 1 \\ & & & & \ddots \\ 0 & & & & \end{vmatrix}. \tag{41}$$

As we have shown in Appendix A in our paper I, $D_{n\sigma}(\nu,k,m)$ and $\tilde{D}_{n\sigma}(\nu,k,m)$ are expanded as follows.

$$D_{n\sigma}(\nu,k,m) = 1 + \sum_{i=1}^{\infty}(-1)^i \sum_{l_1=n}^{\infty}\sum_{l_2=l_1+2}^{\infty}\cdots\sum_{l_i=l_{i-1}+2}^{\infty} a_{l_1\nu+k}(\nu,m)_{\sigma\sigma}a_{l_2\nu+k}(\nu,m)_{\sigma\sigma}\cdots a_{l_i\nu+k}(\nu,m)_{\sigma\sigma}, \tag{42}$$

$$\tilde{D}_{n\sigma}(\nu,k,m) = 1 + \sum_{i=1}^{\infty}(-1)^i \sum_{l_1=n}^{\infty}\sum_{l_2=l_1+2}^{\infty}\cdots\sum_{l_i=l_{i-1}+2}^{\infty} a_{-l_1\nu+k}(\nu,m)_{\sigma\sigma}a_{-l_2\nu+k}(\nu,m)_{\sigma\sigma}\cdots a_{-l_i\nu+k}(\nu,m)_{\sigma\sigma}. \tag{43}$$

Substituting Eq. (37) into Eq. (42), we obtain

$$D_{n\sigma}(\nu,k,m) = \sum_{i=1}^{\infty}\sum_{\alpha_1\gamma_1\cdots\alpha_i\gamma_i}^{0,z} v_{\alpha_1}(\nu,m)v_{\gamma_1}(-\nu,m)\cdots v_{\alpha_i}(\nu,m)v_{\gamma_i}(-\nu,m)\hat{D}^{(i)}_{n\sigma}(\{\alpha\gamma\},\nu,k,m)\ , \tag{44}$$

$$\hat{D}^{(i)}_{n\sigma}(\{\alpha\gamma\},\nu,k,m) = (-1)^i\,\hat{h}_{\alpha_1\gamma_1\sigma}\cdots\hat{h}_{\alpha_i\gamma_i\sigma}A^{(i)}_{n\sigma}(\nu,k,m)\ , \tag{45}$$

$$A^{(i)}_{n\sigma}(\nu,k,m) = \sum_{l_1=n}^{\infty}\sum_{l_2=l_1+2}^{\infty}\cdots\sum_{l_i=l_{i-1}+2}^{\infty} e_{l_1\nu+k\sigma}(\nu,m)e_{l_2\nu+k\sigma}(\nu,m)\cdots e_{l_i\nu+k\sigma}(\nu,m). \tag{46}$$

In the same way, $\tilde{D}_{n\sigma}(\nu,k,m)$ is expressed by Eq. (44) in which $A^{(i)}_{n\sigma}(\nu,k,m)$ has been replaced by

$$\tilde{A}^{(i)}_{n\sigma}(\nu,k,m) = \sum_{l_1=n}^{\infty}\sum_{l_2=l_1+2}^{\infty}\cdots\sum_{l_i=l_{i-1}+2}^{\infty} e_{-l_1\nu+k\sigma}(\nu,m)e_{-l_2\nu+k\sigma}(\nu,m)\cdots e_{-l_i\nu+k\sigma}(\nu,m). \tag{47}$$

The quantities $A^{(i)}_{n\sigma}(\nu,k,m)$ and $\tilde{A}^{(i)}_{n\sigma}(\nu,k,m)$ contain the i-fold summations. In order to reduce these summations, we make use of an asymptotic approximation. The approximation is based on a high-frequency behavior of $\tilde{g}_{L\sigma}(n)$ as

$$\tilde{g}_{L\sigma}(n) = \frac{1}{i\omega_n - \epsilon^0_L + \mu - v_{L\sigma}(0)} + O\left(\frac{1}{(i\omega_n)^3}\right). \tag{48}$$

Then the product of $\tilde{g}_{L\sigma}(n-\nu)$ and $\tilde{g}_{L\sigma}(n)$ in $e_{n\sigma}(\nu,m)$ is written by their difference as

$$e_{n\sigma}(\nu,m) \sim \overline{q}_\nu(\tilde{g}_{L\sigma}(n-\nu) - \tilde{g}_{L\sigma}(n)) \ , \tag{49}$$

where $\overline{q}_\nu = \beta/2\pi\nu i$.

Substituting Eq. (49) into Eq. (46) successively, we find

$$A^{(i)}_{n\sigma}(\nu,k,m) \sim \frac{1}{i\,!}\,\overline{q}^{\,i}_\nu\,\tilde{g}_{L\sigma}((n-1)\nu+k)\tilde{g}_{L\sigma}(n\nu+k)\cdots\tilde{g}_{L\sigma}((n+i-2)\nu+k) \ . \tag{50}$$

In the same way, we have

$$\tilde{A}^{(i)}_{n\sigma}(\nu,k,m) \sim \frac{1}{i\,!}\,\overline{q}^{\,i}_\nu\,\tilde{g}_{L\sigma}(-n\nu+k)\tilde{g}_{L\sigma}(-(n+1)\nu+k)\cdots\tilde{g}_{L\sigma}(-(n+i-1)\nu+k) \ . \tag{51}$$

Substituting $D_{n\sigma}(\nu,k,m)$ with Eq. (50) and $\tilde{D}_{n\sigma}(\nu,k,m)$ with Eq. (51) into Eq. (39), we obtain

$$D_{\nu\sigma}(k,m) = \sum_{l=1}^{\infty}\sum_{\alpha_1\gamma_1\cdots\alpha_l\gamma_l}^{0,z} v_{\alpha_1}(\nu,m)v_{\gamma_1}(-\nu,m)\cdots v_{\alpha_l}(\nu,m)v_{\gamma_l}(-\nu,m)\hat{D}^{(l)}_{\{\alpha\gamma\}\sigma}(\nu,k,m) \ , \tag{52}$$

$$\hat{D}^{(l)}_{\{\alpha\gamma\}\sigma}(\nu,k,m) = \Lambda^{(l)}_\sigma(\{\alpha\gamma\})\frac{\overline{q}^{\,i}_\nu}{l\,!}B^{(l)}_\sigma(\nu,k,m) \ . \tag{53}$$

Here

$$\Lambda^{(l)}_\sigma(\{\alpha\gamma\}) = \begin{cases} 1 & (\sigma =\uparrow) \\ (-1)^{l-n_l(\{\alpha\gamma\})} & (\sigma =\downarrow) \end{cases} \ , \tag{54}$$

$$\begin{aligned} B^{(l)}_\sigma(\nu,k,m) \ = \ & \Big[\prod_{j=0}^{l-1}\tilde{g}_{L\sigma}(j\nu+k)\Big] \\ & + \sum_{i=0}^{l-1}\frac{(-)^{l-i}l!}{i!(l-i)!}\Big[\prod_{j=-(l-i)}^{i-1}\tilde{g}_{L\sigma}(j\nu+k)\Big]\Big[1+\frac{l-i}{\overline{q}^{\,i}_\nu}\tilde{g}_{L\sigma}(i\nu+k)\Big] \ , \end{aligned} \tag{55}$$

and $\hat{D}^{(0)}_{\{\alpha\gamma\}\sigma}(\nu,k,m) = 1$. $n_l(\{\alpha\gamma\})$ in Eq. (54) is the number of $\{\alpha_i\gamma_i\}$ pairs such that $\alpha_i = \gamma_i$ among the l pairs.

Substituting Eq. (52) into Eq. (36), we obtain $\hat{D}^{(n)}_{\{\alpha\gamma\}}(\nu,k,m)$ in the asymptotic approximation.

$$\hat{D}^{(n)}_{\{\alpha\gamma\}}(\nu,k,m) = \sum_{l=0}^{n}\hat{D}^{(l)}_{\{\alpha_1\gamma_1\cdots\alpha_l\gamma_l\}\uparrow}(\nu,k,m)\hat{D}^{(n-l)}_{\{\alpha_{l+1}\gamma_{l+1}\cdots\alpha_n\gamma_n\}\downarrow}(\nu,k,m) \ . \tag{56}$$

Here we wrote the subscript at the r.h.s. explicitly to avoid confusion. Note that the values of α_i and γ_i are limited to 0 or z in the present approximation. When there is no orbital degeneracy, Eq. (55) reduces to the result of the zeroth asymptotic approximation in our paper I[20].

In the actual applications we make use of the exact form up to a certain order of expansion in $\overline{D}^{(m)}_\nu$, and for higher order terms we adopt an approximate form (56). In this way, we can take into account dynamical corrections systematically starting from both sides, the weak interaction limit and the high-temperature one.

IV. NUMERICAL RESULTS OF EXCITATION SPECTRA

In the numerical calculations, we took into account the dynamical corrections up to the second order ($n \le 2$) exactly, and the higher-order terms up to the fourth order within the asymptotic approximation. Summation with respect to ν in Eqs. (28) and (32) was taken up to $\nu = 100$ for $n = 1$ and 2, and up to $\nu = 2$ for $n = 3,\ 4$.

When we solved the CPA equation (31), we adopted a decoupling approximation to the thermal average of impurity Green function[39], *i.e.*,

$$\langle G_{L\sigma}(\xi_z,\xi_\perp^2,i\omega_n)\rangle = \sum_{q=\pm}\frac{1}{2}\left(1+q\frac{\langle\xi_z\rangle}{\sqrt{\langle\xi_z^2\rangle}}\right)G_{L\sigma}(q\sqrt{\langle\xi_z^2\rangle},\langle\xi_\perp^2\rangle,i\omega_n)\ . \tag{57}$$

Here we wrote the static exchange field $\boldsymbol{\xi}$ as $(\xi_z,\xi_\perp^2)$ so that the decoupling approximation we made becomes clearer. The approximation is correct up to the second moment (*i.e.*, $\langle\xi_\alpha^2\rangle$) and allows us to describe the thermal spin fluctuations in a simple way.

On the other hand, we adopted a diagonal approximation[40,41] to the coherent Green function at the r.h.s. of Eq. (31).

$$F_{L\sigma}(n) = \int \frac{\rho_L^{\rm LDA}(\epsilon)d\epsilon}{i\omega_n-\epsilon-\Sigma_{L\sigma}(i\omega_n)-\Delta\epsilon_L}\ . \tag{58}$$

Here $\rho_L^{\rm LDA}(\epsilon)$ is the local density of states for the LDA band calculation, and $\Delta\epsilon_L=(\epsilon_L-\epsilon_L^0)\delta_{l2}$. The approximation partly takes into account the effects of hybridization between different l blocks in the nonmagnetic state, but neglects the effects via spin polarization.

The CPA equation with use of the decoupling approximation (57) yields an approximate solution to the full CPA equation (31). For the calculations of excitation spectra, one needs more accurate solution for the CPA self-consistent equation. We thus adopted the following average t-matrix approximation[16,41] (ATA) after we solved Eq. (31) with the decoupling approximation.

$$\Sigma_{L\sigma}^{\rm ATA}(i\omega_n) = \Sigma_{L\sigma}(i\omega_n)+\frac{\langle G_{L\sigma}(\xi_z,\xi_\perp^2,i\omega_n)\rangle - F_{L\sigma}(i\omega_n)}{\langle G_{L\sigma}(\xi_z,\xi_\perp^2,i\omega_n)\rangle F_{L\sigma}(i\omega_n)}\ . \tag{59}$$

Here the coherent potential in the decoupling approximation is used at the r.h.s., but the full average $\langle\ \rangle$ of the impurity Green function is taken. The ATA is a one-shot correction to the full CPA (31).

The coherent potential $\Sigma_{L\sigma}(z)$ on the real axis $z=\omega+i\delta$ is then calculated by using the Padé numerical analytic continuation method[42]. Here δ is an infinitesimal positive number. The densities of states (DOS) as the single-particle excitations, $\rho_L(\omega)$ are calculated from the relation,

$$\rho_L(\omega) = -\frac{1}{\pi}\,{\rm Im}\,F_{L\sigma}(z)\ . \tag{60}$$

We adopted the same lattice constants and structures as used by Andersen *et. al.*[22] in order to investigate a systematic change of excitations. For fcc Fe, we used the lattice constant 6.928 a.u. being observed at 1440 K. The LDA calculations have been performed with use of the Barth-Hedin exchange-correlation potential to make the TB-LMTO Hamiltonian (2). In the present work all the dynamical CPA calculations have been performed at 2000 K in the paramagnetic state.

We adopted average Coulomb interaction parameters $\overline{U}$ obtained by Bandyopadhyav *et. al.*[43], and the average exchange interactions $\overline{J}$ obtained from the Hartree-Fock atomic calculations[44]. The intra-orbital Coulomb interaction U_0, inter-orbital Coulomb interaction U_1, and the exchange interaction energy parameter J were calculated from $\overline{U}$ and $\overline{J}$ as $U_0=\overline{U}+8\overline{J}/5$, $U_1=\overline{U}-2\overline{J}/5$, and $J=\overline{J}$, using the relation $U_0=U_1+2J$.

Calculated Coulomb interactions from Sc to Cu are plotted in Fig. 1 as a function of the valence electron number n_e. For Fe and Ni, we adopted the values used by Anisimov *et. al.*[36], which are also shown in the figure. Recent calculations suggest that the exchange interactions in the 3d metals are reduced by about 30% as compared with their atomic values[45]. These values are also shown in Fig. 1 by dotted line. We will discuss the screening effects of J on the spectra using the values.

Before we present the results of excitation spectra in 3d series, we briefly discuss the 4th-order dynamical effects. Figure 2 shows the d partial DOS for the paramagnetic bcc Fe on various levels of approximations. The static approximation with the decoupling scheme (57) causes too strong thermal spin fluctuations with large exchange splitting, and yields the two-peak structure as shown by a thin curves in Fig. 2. The second order dynamical corrections suppress the thermal spin fluctuations and reduce the d band width as well as the dip at $\omega=-0.12$ Ry. The 4th-order corrections enhance the two peaks. Finally the ATA correction (the best result in the present work) reduces the peaks and shifts them towards the Fermi level (*i.e.*, the low energy side).

We have reported in our recent paper[46] that the 4th-order dynamical corrections improve the magnetic properties of Fe and Ni. We obtained the Curie temperature $T_{\rm C}=2070$ K (1420 K) for Fe (Ni) in the static approximation. The second-order dynamical corrections lead to $T_{\rm C}=2020$ K (1260 K) for Fe (Ni). The 4th-order dynamical corrections

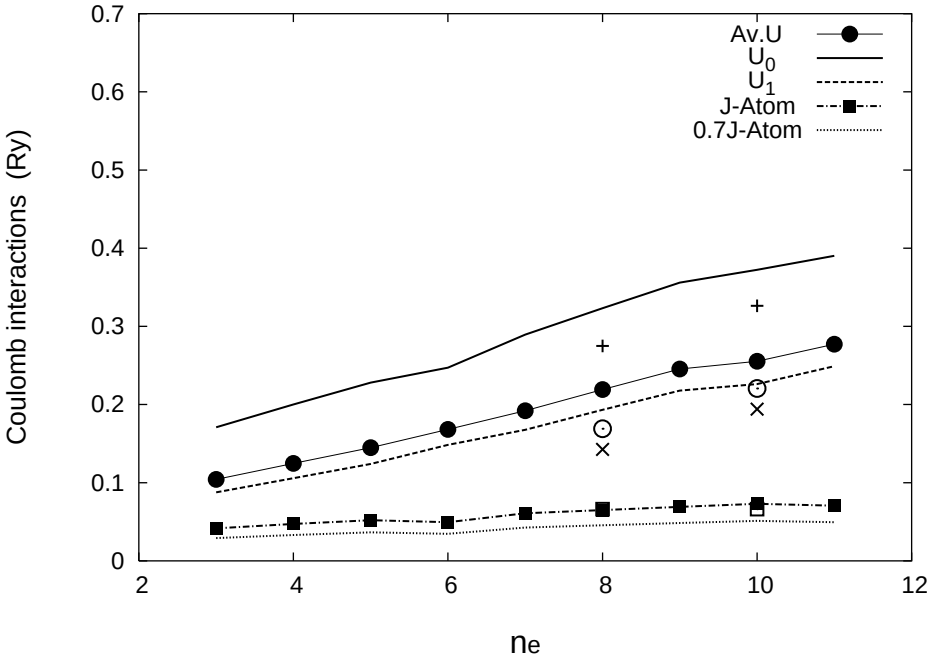

FIG. 1: Intraatomic Coulomb and exchange energy parameters as a function of the conduction electron number of $3d$ transition metals. These parameters are obtained from the band[43] and atomic[44] calculations. Averaged Coulomb interactions $\overline{U}$: closed circles and thin curve, intraorbital Coulomb interactions U_0: solid curve, interorbital Coulomb interactions U_1: dashed curve, Hartree-Fock exchange interactions $\overline{J}$: closed squares and dot-dashed curve, and screened exchange interactions $0.7J$: dotted curve. $\overline{U}$, U_0, U_1, $\overline{J}$ recommended by Anisimov *et. al.*[36] are plotted by ◯, +, ×, and □, respectively, for Fe ($n_e = 8$) and Ni ($n_e = 10$).

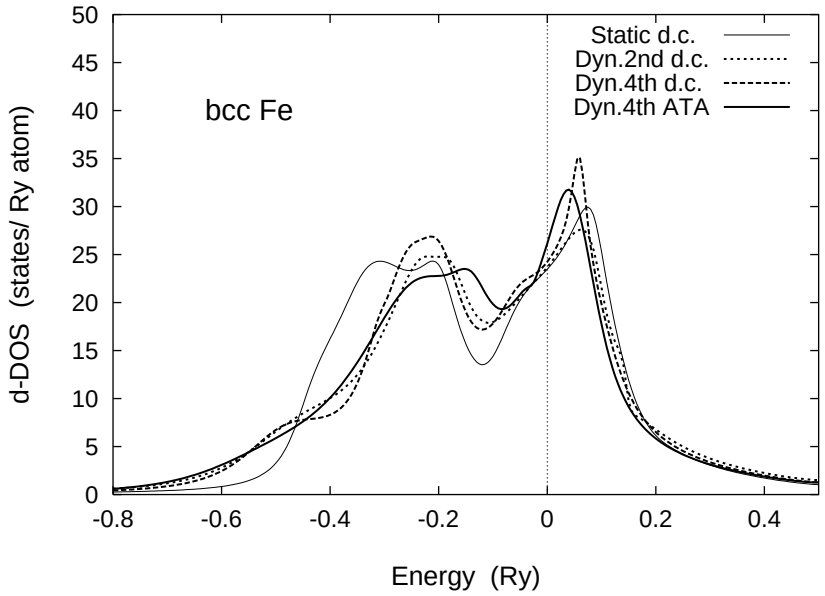

FIG. 2: The d partial densities of states (DOS) of bcc Fe at 2000K in various approximations. The DOS in the static approximation with the decoupling scheme (57): thin solid curve, the DOS with the 2nd-order dynamical corrections and the decoupling (57): dotted curve, the DOS with the 4th-order dynamical corrections and the decoupling (57), and the DOS with the 4th-order dynamical corrections in the ATA.

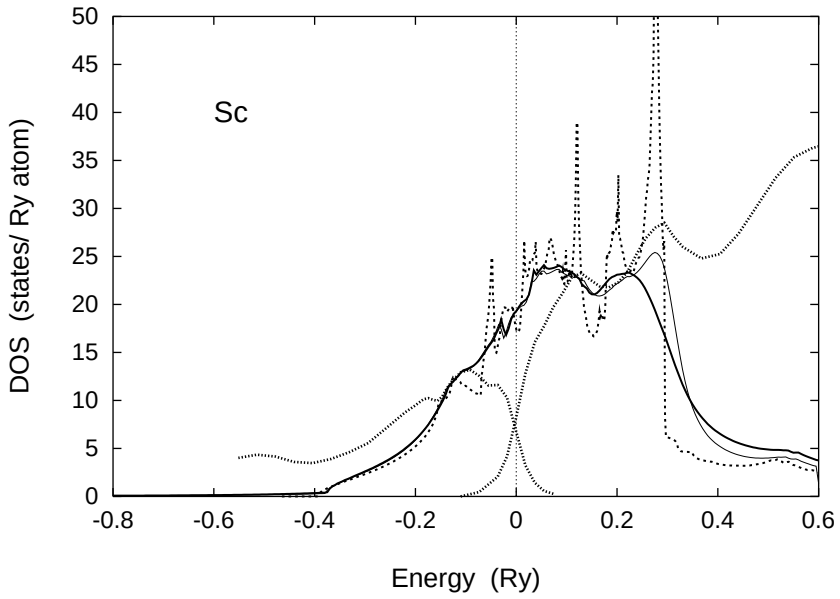

FIG. 3: Densities of states (DOS) as the single-particle excitation spectra for fcc Sc. DOS in the static approximation: thin solid curve, DOS with dynamical correction: solid curve, DOS in the local density approximation (LDA): dashed curve. The X-ray photoemission spectra (XPS)[24] and inverse photoemission spectra (BIS)[25] for hcp Sc at room temperature are shown by dotted curves. Note that these data are arbitrarily renormalized in order to fit the calculated DOS.

further reduce $T_{\rm C}$ to 1930 K for Fe and 620 K for Ni, respectively. The latter is in good agreement with the experimental value 630 K, while the former is still overestimated by a factor of 1.8. A large reduction of $T_{\rm C}$ in Ni due to the 4th-order dynamical corrections has been attributed to a reduction of the DOS at the Fermi level. Calculated effective Bohr magneton numbers in the 2nd-order dynamical CPA are 3.0 $\mu_{\rm B}$ and 1.2 $\mu_{\rm B}$ for Fe and Ni, respectively. The 4th-order dynamical corrections yield 3.0 $\mu_{\rm B}$ for Fe and 1.6 $\mu_{\rm B}$ for Ni, both of which are in good agreement with the experimental values 3.2 $\mu_{\rm B}$ (Fe) and 1.6 $\mu_{\rm B}$ (Ni).

Among the $3d$ transition metals, scandium has the weakest Coulomb interaction as shown in Fig. 1. Calculated DOS for fcc Sc are presented in Fig. 3. The DOS below the Fermi level is close to the LDA DOS except some detailed structures. This is due to a small number of d electrons per orbital (~ 0.3 per d orbital) and rather weak Coulomb interactions. It should be noted that there is no correlation correction to the *sp* bands in the present approximation (58), so that spiky structure of the *sp* bands in the LDA calculations remains in the total DOS. The d DOS are smoothed by the scattering corrections of the self-energy. The corrections become larger near the top of d bands, so that the peak of t_{2g} band at $\omega = 0.275$ Ry is much damped down, the d band becomes narrower, and the spectral weight shifts to the higher energy region. The difference between the dynamical and static DOS is rather small except high energy region ($\omega \gtrsim 0.2$ Ry). We performed the numerical calculations with use of the screened value $\overline{J} = 0.029$ Ry, but we hardly found the change of DOS in shape.

Calculated DOS qualitatively agree with the XPS and BIS data for hcp Sc[24,25] as shown in Fig. 3. (Note that the crystal structure of Sc is not the fcc but the hcp experimentally.) Here and in the followings the intensities of the experimental data are arbitrarily scaled to fit theoretical DOS. Rapid decrease of the XPS and BIS data indicates the cut-off due to Fermi distribution function. Moreover the deviations from the DOS in high energy region are due to secondary electrons, and outside the scope of the present theory. The high-energy peak in the calculated DOS around $\omega = 0.25$ Ry deviates from the BIS peak at $\omega = 0.30$ Ry. This is partly explained by the difference in crystal structure. In fact, the LDA calculations[47] indicate that the peak position in the hcp Sc is higher than that of the fcc one by 0.025 Ry. A small hump at about $\omega = -0.2$ Ry in the XPS data does not appear in the present calculations. The discrepancy is not due to the hcp crystal structure since there is no corresponding peak in the LDA DOS for the hcp Sc[47].

In the case of fcc Ti, we obtained the DOS being similar to the fcc Sc as shown in Fig. 4. Thermal excitations smooth the LDA DOS, damp the highest peak at $\omega = 0.25$ Ry, and transfer the spectral weight to the higher energy region ($\omega \gtrsim 0.30$ Ry). The dynamical corrections are not so important in the case of Ti as understood by comparing the DOS with that in the static approximation. We find rather good agreement of the DOS with both the XPS and BIS experimental data for hcp Ti.

We have calculated the excitation spectra of vanadium for the bcc structure as shown in Fig. 5. In this case the

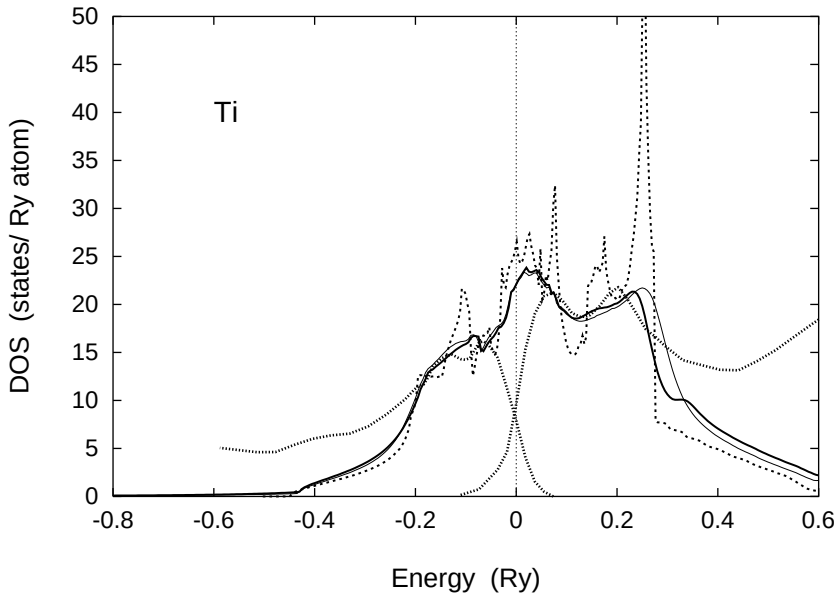

FIG. 4: Calculated DOS for fcc Ti. The notations are the same as in Fig. 3. The XPS[24] and BIS[25] data for the hcp Ti are obtained at room temperature.

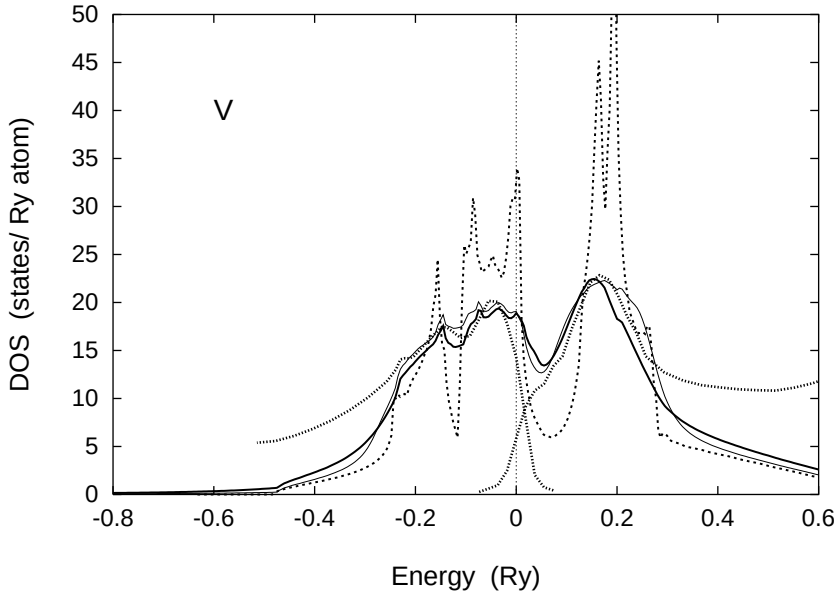

FIG. 5: Calculated DOS for bcc V. The notations are the same as in Fig. 3. The XPS[24] and BIS[25] data for the bcc V are obtained at room temperature.

crystal structure is identical with the experimental one. The main peaks and valleys in the LDA DOS are much weakened by local electron correlations, and the spectral weights move to the higher energy region. The d bands in the quasiparticle energy region ($|\omega| < 0.2$ Ry) shrink by about 10% as compared with the LDA one. The calculated DOS shows a good agreement with the XPS and BIS data[24,25] in lineshape. Note that any artificial parameter is not introduced for comparison between the theory and experiment. The DOS in the static approximation yields an excess d band broadening due to thermal spin fluctuations.

Calculated excitation spectra of the bcc Cr is similar to that in the bcc V as shown in Fig. 6. Because the valence-electron number of Cr is larger than that of V by one, the Fermi level shifts to the higher energy region. The t_{2g} peak around $\omega = -0.15$ Ry in the LDA DOS is weakened, and shifts toward the Fermi level. The position of the e_g peak at $\omega = 0.1$ Ry is not changed, but its weight is much decreased by electron correlations. The static approximation

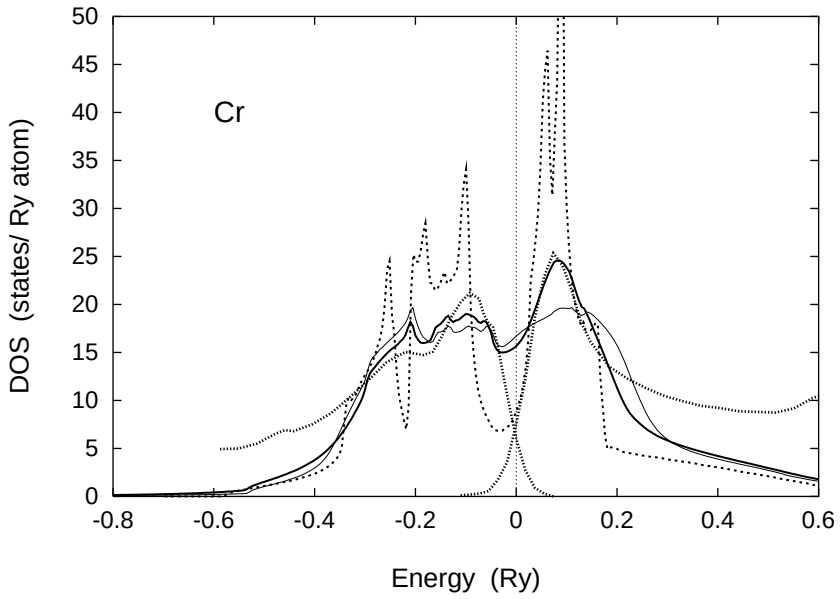

FIG. 6: Calculated DOS for bcc Cr. The notations are the same as in Fig. 3. The XPS[24] and BIS[25] data for the bcc Cr are obtained at room temperature.

broadens the e_g peaks excessively, thus does not explain the BIS data. Calculated peak around $\omega = -0.1$ Ry seems to be too small as compared with the XPS experiment. There is a possibility that the antiferromagnetic correlations enhance the peak in the present calculations, because the experimental data are taken below the Néel temperature.

The Coulomb interactions of Mn are roughly twice as large as those in Sc, while their LDA DOS in the fcc structure are similar to each other. In addition, electron number per atom increases from 3 to 7. Thus one expects more electron correlations in the case of Mn. Calculated DOS as well as experimental XPS-BIS data[24,49] are shown in Fig. 7. We find that the central peak consisting of the t_{2g} bands around $\omega = -0.1$ Ry in the LDA DOS changes to a valley due to electron correlations, so that the DOS shows a two-peak structure. The result indicates a formation of the Mott-Hubbard type bands due to strong on-site correlations as we suggested in our recent paper[48]. The same result was obtained by Birmann *et. al.*[49] by using the Hamiltonian without transverse spin fluctuations. Static approximation overestimates the splitting of the Mott-Hubbard bands. The dynamical effects suppress such a band broadening due to thermal spin fluctuations. When we adopt the screened value $\overline{J} = 0.043$ Ry, the DOS around $\omega = -0.1$ Ry increases and the two-peak structure becomes less clear.

Experimentally, the bulk fcc Mn is realized only in the narrow temperature range between 1352 K and 1407 K at high temperatures. There is no photoemission experiment in this temperature regime. However the XPS data for the 20 monolayer fcc Mn on $Cu_3Au(100)$[49] are available at room temperature. The data seem to be explained by the dynamical CPA with partially screened $\overline{J}$ between 0.043 and 0.061 Ry. Theoretical results agree with the BIS data[25] in peak position.

The line shape of the calculated DOS for bcc Fe is similar to the bcc Cr as shown in Fig. 8. The main peak of the LDA DOS near the Fermi level and the peak of t_{2g} bands around $\omega = -0.15$ Ry are much weakened due to electron correlations. The spectral weight moves to higher energy region. The static approximation overestimates the band width by 20%. The main peak at $\omega = 0.04$ Ry above the Fermi level is consistent with the BIS data[50] at $0.86T_C$, T_C being the Curie temperature. (Note that a hump at $\omega = 0.1$ Ry in the BIS data is the remnant of the e_{2g} peak for the minority band and should disappear above T_C.) On the other hand, the DOS below the Fermi level does not well correspond to the XPS data[51] at $1.03T_C$. One needs more weight around $\omega = -0.1$ Ry in order to explain the experimental data.

The DOS calculated with use of the screened value $\overline{J} = 0.046$ Ry considerably enhance the weight around $\omega = -0.1$ Ry, thus the screening on $\overline{J}$ partly explains the broad peak at $\omega = -0.1$ Ry in the XPS data. This feature does not change even if we adopt $\overline{U}$ value obtained by Bandyopadhyav *et. al.* The magnetic short-range order[52] may also explain the discrepancy between the XPS data and the present result based on the single-site approximation because the experimental data of the XPS are taken near T_C.

We have also investigated the DOS for the fcc Fe. The fcc Fe is well-known to be a typical itinerant magnet showing the spin density waves with magnetic moment of about 1 μ_B per atom at low temperatures[53–55]. But the fcc Fe shows anomalous thermal expansion[56], so that the d band width at high temperatures is expected to become narrower than

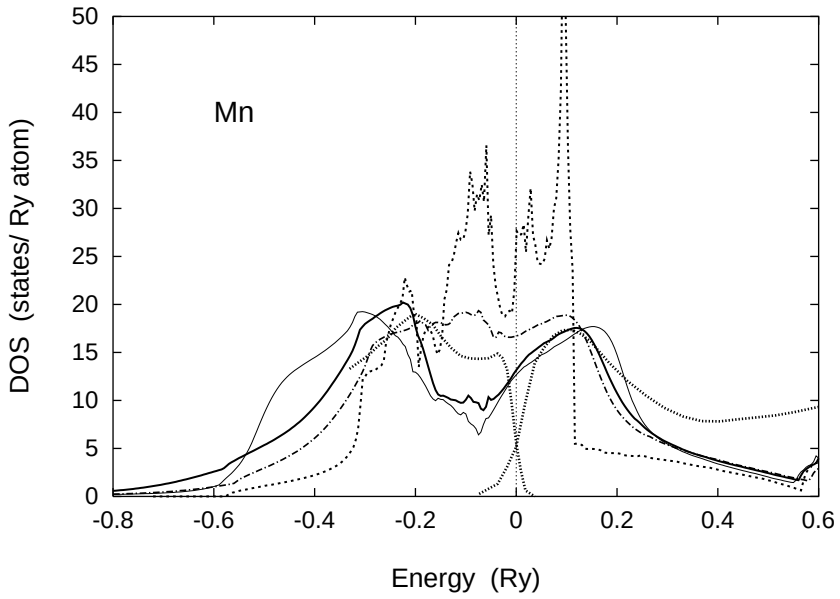

FIG. 7: Calculated DOS for fcc Mn. The notations are the same as in Fig. 3. The dot-dashed curve is the dynamical results for $\overline{U} = 0.192$ Ry and the screened exchange energy parameter $\overline{J} = 0.043$ Ry. The XPS data[49] for the fcc thin-film Mn on $Cu_3Au(100)$ and the BIS data[25] for α-Mn at room temperature are plotted for comparison with the theory.

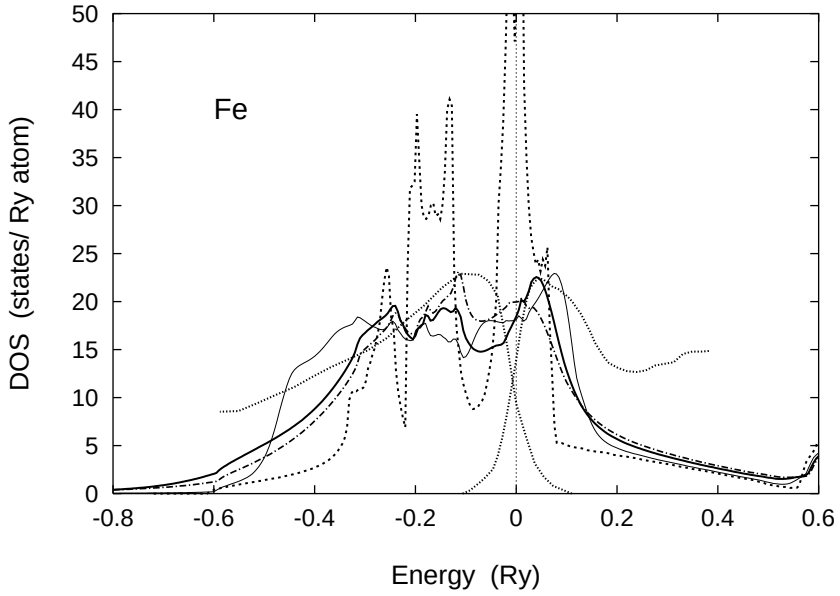

FIG. 8: Calculated DOS for bcc Fe. The notations are the same as in Fig. 3. The dot-dashed curve is the dynamical results for $\overline{U} = 0.169$ Ry and the screened exchange energy parameter $\overline{J} = 0.046$ Ry. The XPS data[51] are measured at $1.03T_{\rm C}$, $T_{\rm C}$ being the Curie temperature. The BIS data[50] are measured at $0.86T_{\rm C}$.

those at low temperatures by several percent. We may then expect stronger correlation effects. As shown in Fig. 9, we find that the DOS calculated with use of the unscreened value $\overline{J} = 0.066$ Ry is similar to that of the fcc Mn. The t_{2g} central peak in the LDA DOS splits into the lower and upper Mott-Hubbard bands due to on-site correlations. The band splittings are smaller than those in the fcc Mn, and the dip at $\omega = -0.15$ Ry is weakened (see Fig. 7). The static approximation overestimates the band width by 20 %.

We present in Fig. 10 the d partial DOS for e_g and t_{2g} bands in order to examine the details of the band splitting. As seen from the figure, both the e_g and the t_{2g} DOS show the two-peak structure. The energy difference between the upper and lower peaks is about 0.25 Ry, which is approximately equal to the intra-orbital Coulomb interaction

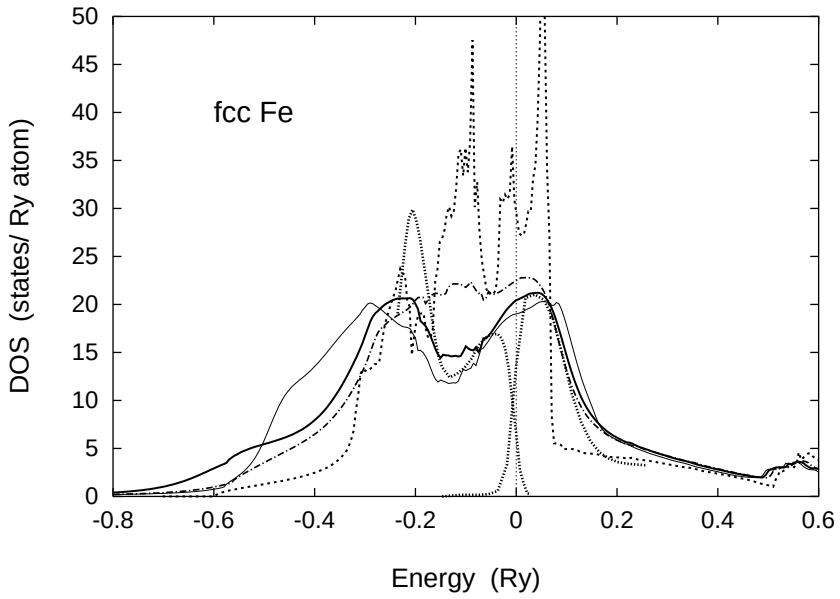

FIG. 9: Calculated DOS for fcc Fe. The notations are the same as in Fig. 3. The dot-dashed curve is the dynamical results for $\overline{U} = 0.169$ Ry and the screened exchange energy parameter $\overline{J} = 0.046$ Ry. The XPS[58] and BIS[57] data are obtained for the fcc Fe on Cu(100) at room temperature.

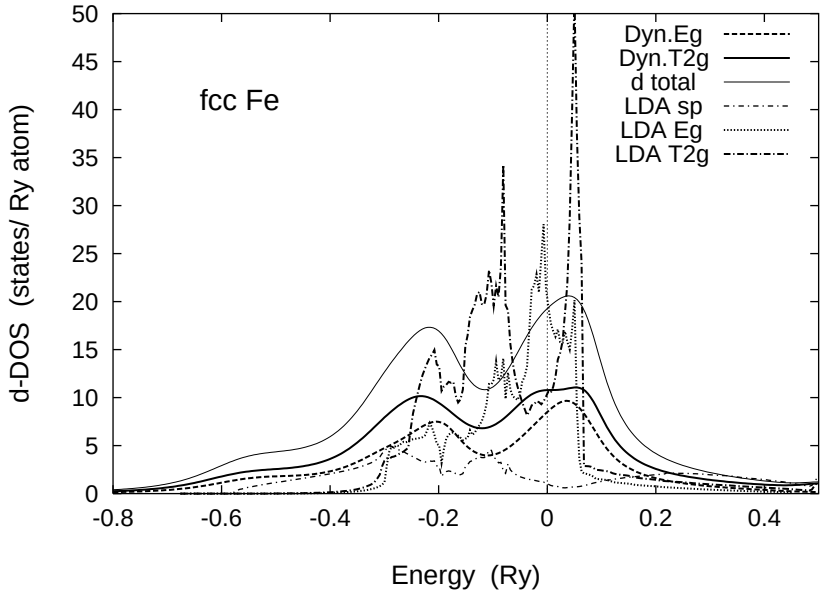

FIG. 10: Partial d DOS of fcc Fe for e_g (dashed curve) and t_{2g} (solid curve) electrons. The total d DOS is shown by thin solid curve. The partial DOS in the LDA are also shown by dotted curve (e_g), dot-dashed curve (t_{2g}), and thin dot-dashed curve (sp electrons), respectively.

for fcc Fe, $U_0 = 0.27$ Ry. Moreover, we find a large scattering peak of $-\mathrm{Im}\Sigma_{L\sigma}(\omega + i\delta)$ at $\omega = -0.12$ Ry. These behaviors verify that the two-peak DOS forms the Mott-Hubbard bands due to electron correlations.

It is remarkable that the dynamical results are sensitive to the choice of $\overline{U}$ and $\overline{J}$ in the case of fcc Fe. The two-peak structure almost disappears when we adopt $\overline{U} = 0.169$ Ry and the screened value $\overline{J} = 0.046$ Ry, as shown in Fig. 9, while it again appears when we adopt $\overline{U} = 0.219$ Ry obtained by Bandhyopadhyav it et. al. and the screened value $\overline{J} = 0.046$ Ry. The behaviors are understood from the following arguments. The Coulomb interactions suppress the doubly occupied states of electrons on an orbital in general. The Hund-rule coupling $\overline{J}$ also suppresses the doubly occupied states to reduce the energy; $\overline{J}$ tends to enhance $\overline{U}$ effectively. Thus the increment of $\overline{U}$ or $\overline{J}$ is favorable for

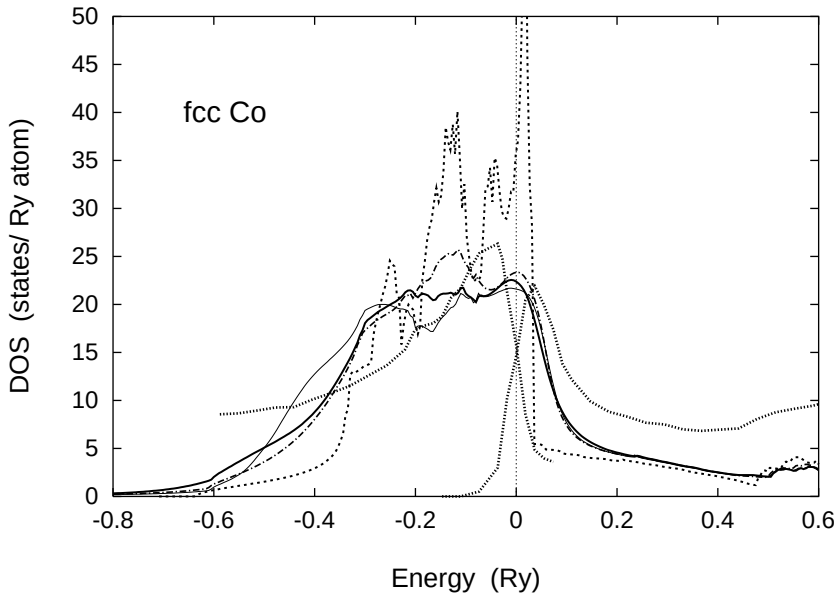

FIG. 11: Calculated DOS for fcc Co. The notations are the same as in Fig. 3. The dot-dashed curve is the dynamical results for $\overline{U} = 0.245$ Ry and the screened exchange energy parameter $\overline{J} = 0.048$ Ry. The XPS[24] and BIS[25] data for the hcp Co at room temperature are drawn by the dotted curves.

the formation of the Mott-Hubbard bands.

The peak near the Fermi level explains well the BIS data[57] for the fcc Fe on Cu(100). The XPS data[58] for the fcc Fe on Cu(100) are somewhat controversial. The peak around $\omega = -0.2$ Ry is usually interpreted as a peak due to Cu substrate. If this peak originates in the Cu substrate by 100%, the data support the result for $(\overline{U}, \overline{J}) = (0.169, 0.046)$ Ry. But if the peak is interpreted as a superposition of both the fcc Fe and the Cu substrate spectra, we expect a two-peak structure of fcc Fe, and the XPS data are consistent with the results for $(\overline{U}, \overline{J}) = (0.169, 0.066)$ and $(\overline{U}, \overline{J}) = (0.219, 0.046)$ Ry. Resolving the problem is left for future investigations.

The DOS of fcc Co in the paramagnetic state does not show the Mott-Hubbard type structure any more as shown in Fig. 11. The peak of the t_{2g} bands at $\omega = -0.15$ Ry becomes almost flat, and the peak of the t_{2g} bands on the Fermi level is much weakened. We find a weak hump around $\omega = -0.5$ Ry suggesting the '6 eV' satellite. When we adopt the screened value $\overline{J} = 0.048$ Ry, the peak at $\omega = -0.15$ Ry partially remains as found in Fig. 11, and the hump around $\omega = -0.5$ Ry almost disappear.

We present in Fig. 12 the e_g and t_{2g} partial DOS to clarify the disappearance of the two-peak structure in the total DOS. Calculated t_{2g} partial DOS does not show the band splitting any more. The e_g DOS still show the two-peak structure. But the dip between the peaks is shallower than that of the fcc Fe (see Fig. 10) and the energy difference between the peaks (0.18 Ry) is smaller than the intra-orbital Coulomb interaction energy $U_0 = 0.36$ Ry. In the case of Co, the number of hole states is reduced as compared with that of fcc Fe. This reduces the charge fluctuations and thus the magnitude of the self-energy by a factor of two. The reduction yields the disappearance of the two-peak structure in the total DOS.

There is no experimental data on the fcc Co above the Curie temperature. Calculated DOS does not show a good agreement with the XPS[24] and BIS data[25] of hcp Co at room temperature. The UPS (Ultraviolet Photoemission Spectroscopy) data for hcp Co by Heimann *et. al.*[59] show the existence of the 6 eV satellite in agreement with the present result for the unscreened $\overline{J}$, while the other data[24,60] do not.

Single-particle excitations of Ni have been investigated extensively in both theory[21,61–65] and experiment[66–70]. Present result of fcc Ni shows a single-peak structure as shown in Fig. 13. Moreover the correlations increase the spectral weight around $\omega = -0.45$ Ry, and creates a small hump corresponding to the 6 eV satellite due to two-hole excitations. The dynamical effects suppress the band broadening of the static approximation by 20 %. These behaviors do not change even if we adopt the screened value $\overline{J} = 0.046$ Ry. The screened $\overline{J}$ enhances the main peak around $\omega = -0.05$ Ry and creates a hump at $\omega = -0.15$ Ry in the DOS. Though the calculated DOS is consistent with the XPS[24] and BIS data[25], the band width seems to be somewhat larger than that of the XPS data.

We present finally in Fig. 14 the DOS for Cu. Electron correlations via a small number of d holes (≈ 0.36 per atom) move the spectral weight of the LDA DOS to the lower energy region. The peak of the d bands shifts toward lower energy by 0.05 Ry. It is also remarkable that a broad hump appears at $\omega = -0.7$ Ry due to two-hole excitations. We

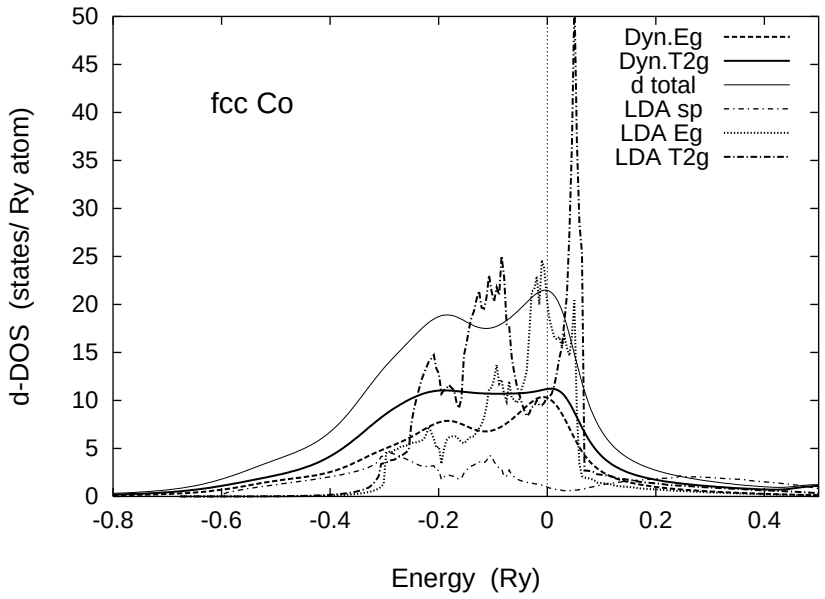

FIG. 12: Partial d DOS of fcc Co for e_g (dashed curve) and t_{2g} (solid curve) electrons. The total d DOS is shown by thin solid curves. The partial DOS in the LDA are also shown by dotted curve (e_g), dot-dashed curve (t_{2g}), and thin dot-dashed curve (sp electrons).

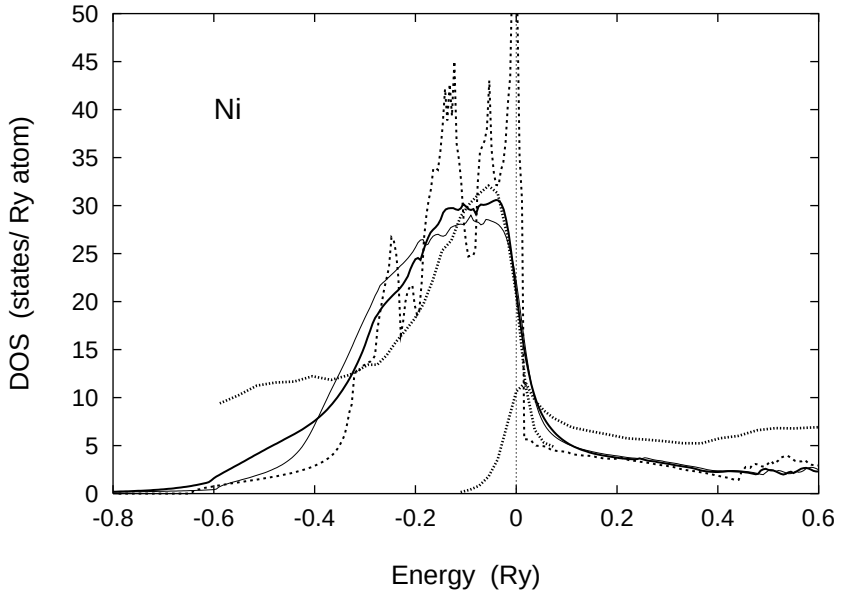

FIG. 13: Calculated DOS for fcc Ni. The notations are the same as in Fig. 3. The XPS[24] and BIS[25] data for the fcc Ni are obtained at room temperature.

find a good agreement between the dynamical CPA theory and the experiment[24,25] for this system.

V. SUMMARY

In the present paper, we have obtained approximate expression of the higher-order dynamical corrections to the effective potential in the first principles dynamical CPA, making use of an asymptotic approximation. The approximation becomes exact in the high frequency limit, and much reduces the multiple summations with respect to the Matsubara frequency at each order of expansion in the dynamical corrections.

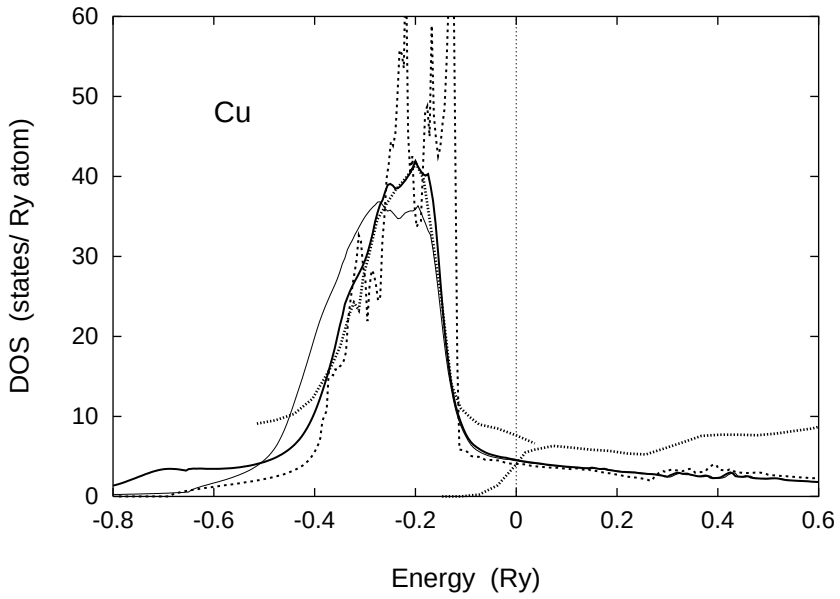

FIG. 14: Calculated DOS for fcc Cu. The notations are the same as in Fig. 3. The XPS[24] and BIS[25] data for the fcc Cu are obtained at room temperature.

Within the 4-th order dynamical corrections, we have investigated systematic change of the DOS at high temperatures in 3d series from Sc to Cu. Thermal spin fluctuations in the static approximation smooth the LDA DOS at high temperatures, especially reduce their main peaks and broaden the d band width. Dynamical effects reduce the band broadening, and move the spectral weight to higher energy region. These effects explain in many cases the lineshape of the XPS and BIS experimental data from Sc to Cu quantitatively or semiquantitatively. We found the formation of the Mott-Hubbard type bands due to electron correlations in the case of fcc Mn and fcc Fe, and also found that the dynamical effects can create a small hump corresponding to '6 eV' satellite in Co, Ni, and Cu.

We investigated the effects of the screened exchange energy parameters using the reduced values of $\overline{J}$ by 30 %. The screening of $\overline{J}$ is significant for the DOS in Mn, Fe, and Co. The reduction of $\overline{J}$ tends to weaken the Mott-Hubbard type bands in fcc Mn, and even could destroy the two-peak structure in the case of fcc Fe. It also develops the central peak around $\omega = -0.1$ Ry in bcc Fe and fcc Co. Some of these results explain better the XPS data. But we have to calculate the other physical quantities with use of the same scheme, and have to examine in more details the consistency among them in order to conclude the validity of the screened values of $\overline{J}$. The magnetic short-range order should also be important for understanding the experimental data of magnetic transition metals for more detailed discussions.

Present theory explains a systematic change of the spectra in 3d series at high temperatures. At lower temperatures, the higher-order dynamical corrections should be more important. Improvements of the theory in the low temperature region are left for future investigations.

Acknowledgments

Numerical calculations have been partly carried out with use of the Hitachi SR11000 in the Supercomputer Center, Institute of Solid State Physics, University of Tokyo.

---

† yok@sci.u-ryukyu.ac.jp

[1] See for example, *Electron Correlations in Molecules and Solids* by P. Fulde (Springer, Berlin, 1995).
[2] M. C. Gutzwiller, Phys. Rev. Lett. **10**, 159 (1963).
[3] M.C. Gutzwiller, Phys. Rev. **134**, A923 (1964).
[4] M.C. Gutzwiller, Phys. Rev. **137**, A1726 (1965).
[5] J. Hubbard, Proc. R. Soc. London A**276**, 238 (1963).

[6] J. Hubbard: Proc. Roy. Soc. (London) A **281**, 401 (1964).
[7] J. Kanamori, Prog. Theor. Phys. **30**, 275 (1963).
[8] M. Cyrot, J. Phys. (Paris) **33**, 25 (1972).
[9] R. L. Stratonovich, Dokl. Akad. Nauk. SSSR **115**, 1097 (1958) [Sov. Phys. - Dokl. **2**, 416 (1958)].
[10] J. Hubbard, Phys. Rev. Lett. **3**, 77 (1959).
[11] W. E. Evenson, J. R. Schrieffer, and S. Q. Wang, J. Appl. Phys. **41**, 1199 (1970); J. R. Schrieffer, W. E. Evenson, and S. Q. Wang, J. Phys. (Paris) Colloq. **32**, C1-19 (1971).
[12] G. Morandi, E. Galleani D'Agliano, F. Napoli, and C. F. Ratto, Adv. Phys. **23**, 867 (1974).
[13] J. Hubbard, Phys. Rev. B**19**, 2626 (1979); **20**, 4584 (1979); **23**, 5974 (1981).
[14] H. Hasegawa, J. Phys. Soc. Jpn. **46**, 1504 (1979); **49**, 178 (1980).
[15] P. Soven, Phys. Rev. **156**, 809 (1967).
[16] H. Ehrenreich and L. M. Schwarz, Solid State Physics, edited by H. Ehrenreich, F. Seitz, and D. Turnbull (Academic, New York, 1976), Vol. 31, p.150.
[17] See for example, R. G. Parr and W. Yang, *Density Functional Theory of Atoms and Molecules* (Oxford University Press., Oxford, 1989).
[18] Y. Kakehashi and P. Fulde, Phys. Rev. B **32**, 1595 (1985).
[19] Y. Kakehashi, Phys. Rev. B **45**, 7196 (1992).
[20] Y. Kakehashi, Phys. Rev. B **65**, 184420 (2002).
[21] Y. Kakehashi, J. Phys. Soc. Jpn **77**, 094706 (2008).
[22] O.K. Andersen, O. Jepsen, and G. Krier: in *Methods of Electronic Structure Calculations* ed. by V. Kumar, O.K. Andersen, and A. Mookerjee (World Scientific Pub., Singapore, 1994) p. 63.
[23] V.I. Anisimov, A.I. Poteryaev, M.A. Korotin, A.O. Anokhin, and G. Kotliar, J. Phys. Condens. Matter **9** (1997) 7359.
[24] A.G. Narmonev and A.I. Zakharov, Phys. Met. Metallogr. **65**, 315 (1988).
[25] W. Speier, J.C. Fuggle, R. Zeller, B. Ackermann, K. Szot, F.U. Hilebrecht, and M. Campagna, Phys. Rev. B **30**, 6921 (1984).
[26] K.D. Belashchenko, V.P. Antropov, N.E. Zein, Phys. Rev. B **73**, 073105 (2006).
[27] Y. Kakehashi: Phys. Rev. B **66** (2002) 104428.
[28] Y. Kakehashi: Adv. in Phys. **53**, 497 (2004); Phil. Mag. **86**, 2603 (2006).
[29] S. Hirooka and M. Shimizu, J. Phys. Soc. Jpn. **43**, 70 (1977).
[30] E. Müller-Hartmann: Z. Phys. B **74** (1989) 507.
[31] M. Jarrell: Phys. Rev. Lett. **69** (1992) 168; M. Jarrell and H.R. Krishnamurthy: Phys. Rev. B **63** (2001) 125102.
[32] A. Georges and G. Kotliar: Phys. Rev. B **45** (1992) 6479; A. Georges and W. Krauth: Phys. Rev. B **48** (1993) 7167.
[33] A. Georges, G. Kotliar, W. Krauth, and M. J. Rozenberg: Rev. Mod. Phys. **68** (1996) 13.
[34] Y. Kakehashi and P. Fulde, Phys. Rev. B **69**, 045101 (2004).
[35] J.E. Hirsch and R.M. Fye: Phys. Rev. Lett. **56** (1989) 2521.
[36] V.I. Anisimov, F. Aryasetiawan, and A.I. Lichtenstein: J. Phys. Condens. Matter **9** (1997) 767.
[37] D.J. Amit and C.M. Bender, Phys. Rev. B **4**, 3115 (1971); D.J. Amit and H.J. Keiter, Low Temp. Phys. **11**, 603 (1973).
[38] Dai Xianxi, J. Phys. Condens. Matter. **3**, 4389 (1991).
[39] Y. Kakehashi, J. Phys. Soc. Jpn., **50**, 1505 (1981); J. Phys. Soc. Jpn., **50**, 2251 (1981).
[40] S. Kirkpatrick, B. Velický, and H. Ehrenreich, Phys. Rev. B **1**, 3250 (1970).
[41] J. Korringa, J. Phys. Chem. Solids **7**, 252 (1958).
[42] H.J. Vidberg and J.W. Serene: J. Low Temp. Phys. **29**, 179 (1977).
[43] T. Bandyopadhyav and D.D. Sarma, Phys. Rev. B **39**, 3517 (1989).
[44] J.B. Mann, Los Alamos Scientific Laboratory Rep. No. LASL-3690 (1967).
[45] T. Miyake and F. Aryasetiawan, Phys. Rev. B **77**, 085122 (2008).
[46] Y. Kakehashi, T. Tamashiro, M.A.R. Patoary, and T. Nakamura, J. Phys. Conf. Series **200**, 032030 (2010).
[47] P. Blaha, K. Schwarz, and P.H. Dederichs, Phys. Rev. B **38**, 9368 (1988).
[48] Y. Kakehashi, M.A.R. Patoary, and T. Tamashiro, J. Phys. Soc. Jpn. **78**, 093705 (2009).
[49] S. Biermann, A. Dallmeyer, C. Carbone, W. Eberhardt, C. Pampuch, O. Rader, M.I. Katsunelson, and A.I. Lichtenstein, condmat/0112430v1 (2001).
[50] J. Kirschner, M. Glöbl, V. Dose, and H. Scheidt, Phys. Rev. Lett. **53**, 612 (1984).
[51] R.E. Kirby, E. Kisker, F.K. King, and E.L. Garwin, Solid. State Commun. **56**, 425 (1985).
[52] E. Kisker, *3d-Metallic Magnetism and Spin-Resolved Photoemission* in *Metallic Magnetism* ed. H. Capellmann (Springer-Verlag, Berlin, 1987) Chap. 3.
[53] Y. Tsunoda, J. Phys. Condens. Matter **1**, 10427 (1989).
[54] Y. Kakehashi, O. Jepsen, and N. Kimura, Phys. Rev. B **65**, 134418 (2002).
[55] T. Uchida, Y. Kakehashi, J. Phys. Soc. Jpn. **75**, 094703 (2006).
[56] P. Chevenard, Rev. de Mét. **25**, 14 (1928).
[57] F.J. Himpsel, Phys. Rev. Lett. **67**, 2363 (1991).
[58] M. Zharnikov, A. Dittschar, W. Kuch, C.M. Schneider, and J. Kirschner, J. Magn. Magn. Mater. **165**, 250 (1997).
[59] P. Heimann, E. Marschall, H. Neddermeyer, M. Pessa, and H.F. Roloff, Phys. Rev. B 16, 2575 (1977).
[60] S. Hüfner and G.K. Wertheim, Phys. Lett. A **47**, 349 (1974).
[61] D.R. Penn: Phys. Rev. Lett. **42** (1979) 921.
[62] A. Liebsch: Phys. Rev. Lett. **43** (1979) 1431; Phys. Rev. B **23** (1981) 5203.
[63] R. H. Victora and L. M. Falicov, Phys. Rev. Lett. **55**, 1140 (1985).

[64] P. Unger, J. Igarashi, and P. Fulde, Phys. Rev. B **50**, 10485 (1994).
[65] A.I. Lichtenstein and M.I. Katsnelson, and G. Kotliar, Phys. Rev. Lett. **87**, 067205 (2001).
[66] D. E. Eastman, F. J. Himpsel, and J. A. Knapp, Phys. Rev. Lett. **40**, 1514 (1978); F. J. Himpsel, J. A. Knapp, and D. E. Eastman, Phys. Rev. B **19**, 2919 (1979).
[67] F.J. Himpsel, J.A. Knapp, and D.E. Eastman, Phys. B **19**, 2919 (1979).
[68] D. E. Eastman, F. J. Himpsel, and J. A. Knapp, Phys. Rev. Lett. **44**, 95 (1980).
[69] W. Eberhardt and E. W. Plummer, Phys. Rev. B 21, 3245 (1980).
[70] H. Martensson and P.O. Nilsson, Phys. Rev. B **30**, 3047 (1984).